Amplitude analysis of the $D_s^+ \to \pi^+\pi^-\pi^+$ decay

M. Ablikim[1], M. N. Achasov[10,b], P. Adlarson[66], S. Ahmed[14], M. Albrecht[4], R. Aliberti[27], A. Amoroso[65A,65C], M. R. An[31], Q. An[62,48], X. H. Bai[56], Y. Bai[47], O. Bakina[28], R. Baldini Ferroli[22A], I. Balossino[23A], Y. Ban[37,h], K. Begzsuren[25], N. Berger[27], M. Bertani[22A], D. Bettoni[23A], F. Bianchi[65A,65C], J. Bloms[59], A. Bortone[65A,65C], I. Boyko[28], R. A. Briere[5], H. Cai[67], X. Cai[1,48], A. Calcaterra[22A], G. F. Cao[1,53], N. Cao[1,53], S. A. Cetin[52A], J. F. Chang[1,48], W. L. Chang[1,53], G. Chelkov[28,a], D. Y. Chen[6], G. Chen[1], H. S. Chen[1,53], M. L. Chen[1,48], S. J. Chen[34], X. R. Chen[24], Y. B. Chen[1,48], Z. J Chen[19,i], W. S. Cheng[65C], G. Cibinetto[23A], F. Cossio[65C], X. F. Cui[35], H. L. Dai[1,48], X. C. Dai[1,53], A. Dbeyssi[14], R. E. de Boer[4], D. Dedovich[28], Z. Y. Deng[1], A. Denig[27], I. Denysenko[28], M. Destefanis[65A,65C], F. De Mori[65A,65C], Y. Ding[32], C. Dong[35], J. Dong[1,48], L. Y. Dong[1,53], M. Y. Dong[1,48,53], X. Dong[67], S. X. Du[70], Y. L. Fan[67], J. Fang[1,48], S. S. Fang[1,53], Y. Fang[1], R. Farinelli[23A], L. Fava[65B,65C], F. Feldbauer[4], G. Felici[22A], C. Q. Feng[62,48], J. H. Feng[49], M. Fritsch[4], C. D. Fu[1], Y. Gao[63], Y. Gao[62,48], Y. Gao[37,h], Y. G. Gao[6], I. Garzia[23A,23B], P. T. Ge[67], C. Geng[49], E. M. Gersabeck[57], A Gilman[60], K. Goetzen[11], L. Gong[32], W. X. Gong[1,48], W. Gradl[27], M. Greco[65A,65C], L. M. Gu[34], M. H. Gu[1,48], C. Y Guan[1,53], A. Q. Guo[21], L. B. Guo[33], R. P. Guo[39], Y. P. Guo[9,f], A. Guskov[28,a], T. T. Han[40], W. Y. Han[31], X. Q. Hao[15], F. A. Harris[55], K. L. He[1,53], F. H. Heinsius[4], C. H. Heinz[27], Y. K. Heng[1,48,53], C. Herold[50], M. Himmelreich[11,d], T. Holtmann[4], G. Y. Hou[1,53], Y. R. Hou[53], Z. L. Hou[1], H. M. Hu[1,53], J. F. Hu[46,j], T. Hu[1,48,53], Y. Hu[1], G. S. Huang[62,48], L. Q. Huang[63], X. T. Huang[40], Y. P. Huang[1], Z. Huang[37,h], T. Hussain[64], N Hüsken[21,27], W. Ikegami Andersson[66], W. Imoehl[21], M. Irshad[62,48], S. Jaeger[4], S. Janchiv[25], Q. Ji[1], Q. P. Ji[15], X. B. Ji[1,53], X. L. Ji[1,48], Y. Y. Ji[40], H. B. Jiang[40], X. S. Jiang[1,48,53], J. B. Jiao[40], Z. Jiao[17], S. Jin[34], Y. Jin[56], M. Q. Jing[1,53], T. Johansson[66], N. Kalantar-Nayestanaki[54], X. S. Kang[32], R. Kappert[54], M. Kavatsyuk[54], B. C. Ke[42,1], I. K. Keshk[4], A. Khoukaz[59], P. Kiese[27], R. Kiuchi[1], R. Kliemt[11], L. Koch[29], O. B. Kolcu[52A], B. Kopf[4], M. Kuemmel[4], M. Kuessner[4], A. Kupsc[66], M. G. Kurth[1,53], W. Kühn[29], J. J. Lane[57], J. S. Lange[29], P. Larin[14], A. Lavania[20], L. Lavezzi[65A,65C], Z. H. Lei[62,48], H. Leithoff[27], M. Lellmann[27], T. Lenz[27], C. Li[38], C. H. Li[31], Cheng Li[62,48], D. M. Li[70], F. Li[1,48], G. Li[1], H. Li[42], H. Li[62,48], H. B. Li[1,53], H. J. Li[15], J. L. Li[40], J. Q. Li[4], J. S. Li[49], Ke Li[1], L. K. Li[1], Lei Li[3], P. R. Li[30,k,l], S. Y. Li[51], W. D. Li[1,53], W. G. Li[1], X. H. Li[62,48], X. L. Li[40], Xiaoyu Li[1,53], Z. Y. Li[49], H. Liang[1,53], H. Liang[62,48], H. Liang[26], Y. F. Liang[44], Y. T. Liang[24], G. R. Liao[12], L. Z. Liao[1,53], J. Libby[20], A. Limphirat[50], C. X. Lin[49], T. Lin[1], B. J. Liu[1], C. X. Liu[1], D. Liu[14,62], F. H. Liu[43], Fang Liu[1], Feng Liu[6], H. M. Liu[1,53], Huanhuan Liu[1], Huihui Liu[16], J. B. Liu[62,48], J. L. Liu[63], J. Y. Liu[1,53], K. Liu[1], K. Y. Liu[32], Ke Liu[6], L. Liu[62,48], M. H. Liu[9,f], P. L. Liu[1], Q. Liu[67], Q. Liu[53], S. B. Liu[62,48], Shuai Liu[45], T. Liu[9,f], T. Liu[1,53], W. M. Liu[62,48], X. Liu[30,k,l], Y. Liu[30,k,l], Y. B. Liu[35], Z. A. Liu[1,48,53], Z. Q. Liu[40], X. C. Lou[1,48,53], F. X. Lu[49], H. J. Lu[17], J. D. Lu[1,53], J. G. Lu[1,48], X. L. Lu[1], Y. Lu[1], Y. P. Lu[1,48], C. L. Luo[33], M. X. Luo[69], P. W. Luo[49], T. Luo[9,f], X. L. Luo[1,48], X. R. Lyu[53], F. C. Ma[32], H. L. Ma[1], L. L. Ma[40], M. M. Ma[1,53], Q. M. Ma[1], R. Q. Ma[1,53], R. T. Ma[53], X. X. Ma[1,53], X. Y. Ma[1,48], F. E. Maas[14], M. Maggiora[65A,65C], S. Maldaner[4], S. Malde[60], Q. A. Malik[64], A. Mangoni[22B], Y. J. Mao[37,h], Z. P. Mao[1], S. Marcello[65A,65C], Z. X. Meng[56], J. G. Messchendorp[54], G. Mezzadri[23A], T. J. Min[34], R. E. Mitchell[21], X. H. Mo[1,48,53], N. Yu. Muchnoi[10,b], H. Muramatsu[58], S. Nakhoul[11,d], Y. Nefedov[28], F. Nerling[11,d], I. B. Nikolaev[10,b], Z. Ning[1,48], S. Nisar[8,g], S. L. Olsen[53], Q. Ouyang[1,48,53], S. Pacetti[22B,22C], X. Pan[9,f], Y. Pan[57], A. Pathak[1], A. Pathak[26], P. Patteri[22A], M. Pelizaeus[4], H. P. Peng[62,48], K. Peters[11,d], J. Pettersson[66], J. L. Ping[33], R. G. Ping[1,53], S. Pogodin[28], R. Poling[58], V. Prasad[62,48], H. Qi[62,48], H. R. Qi[51], K. H. Qi[24], M. Qi[34], T. Y. Qi[9], S. Qian[1,48], W. B. Qian[53], Z. Qian[49], C. F. Qiao[53], L. Q. Qin[12], X. P. Qin[9], X. S. Qin[40], Z. H. Qin[1,48], J. F. Qiu[1], S. Q. Qu[35], K. H. Rashid[64], K. Ravindran[20], C. F. Redmer[27], A. Rivetti[65C], V. Rodin[54], M. Rolo[65C], G. Rong[1,53], Ch. Rosner[14], M. Rump[59], H. S. Sang[62], A. Sarantsev[28,c], Y. Schelhaas[27], C. Schnier[4], K. Schoenning[66], M. Scodeggio[23A,23B], D. C. Shan[45], W. Shan[18], X. Y. Shan[62,48], J. F. Shangguan[45], M. Shao[62,48], C. P. Shen[9], H. F. Shen[1,53], P. X. Shen[35], X. Y. Shen[1,53], H. C. Shi[62,48], R. S. Shi[1,53], X. Shi[1,48], X. D Shi[62,48], J. J. Song[40], W. M. Song[26,1], Y. X. Song[37,h], S. Sosio[65A,65C], S. Spataro[65A,65C], K. X. Su[67], P. P. Su[45], F. F. Sui[40], G. X. Sun[1], H. K. Sun[1], J. F. Sun[15], L. Sun[67], S. S. Sun[1,53], T. Sun[1,53], W. Y. Sun[26], W. Y. Sun[33], X Sun[19,i], Y. J. Sun[62,48], Y. Z. Sun[1], Z. T. Sun[1], Y. H. Tan[67], Y. X. Tan[62,48], C. J. Tang[44], G. Y. Tang[1], J. Tang[49], J. X. Teng[62,48], V. Thoren[66], W. H. Tian[42], Y. T. Tian[24], I. Uman[52B], B. Wang[1], C. W. Wang[34], D. Y. Wang[37,h], H. J. Wang[30,k,l], H. P. Wang[1,53], K. Wang[1,48], L. L. Wang[1], M. Wang[40], M. Z. Wang[37,h], Meng Wang[1,53], S. Wang[9,f], W. Wang[49], W. H. Wang[67], W. P. Wang[62,48], X. Wang[37,h], X. F. Wang[30,k,l], X. L. Wang[9,f], Y. Wang[49], Y. Wang[62,48], Y. D. Wang[36], Y. F. Wang[1,48,53], Y. Q. Wang[1], Y. Y. Wang[30,k,l], Z. Wang[1,48], Z. Y. Wang[1], Ziyi Wang[53], Zongyuan Wang[1,53], D. H. Wei[12], F. Weidner[59], S. P. Wen[1], D. J. White[57], U. Wiedner[4], G. Wilkinson[60], M. Wolke[66], L. Wollenberg[4], J. F. Wu[1,53], L. H. Wu[1], L. J. Wu[1,53], X. Wu[9,f], Z. Wu[1,48], L. Xia[62,48], H. Xiao[9,f], S. Y. Xiao[1], Z. J. Xiao[33], X. H. Xie[37,h], Y. G. Xie[1,48], Y. H. Xie[6], T. Y. Xing[1,53], C. J. Xu[49], G. F. Xu[1], Q. J. Xu[13], W. Xu[1,53], X. P. Xu[45], Y. C. Xu[53], F. Yan[9,f], L. Yan[9,f], W. B. Yan[62,48], W. C. Yan[70], Xu Yan[45], H. J. Yang[41,e], H. X. Yang[1], L. Yang[42], S. L. Yang[53], Y. X. Yang[12], Yifan Yang[1,53], Zhi Yang[24], M. Ye[1,48], M. H. Ye[7], J. H. Yin[1], Z. Y. You[49], B. X. Yu[1,48,53], C. X. Yu[35], G. Yu[1,53], J. S. Yu[19,i], T. Yu[63], C. Z. Yuan[1,53], L. Yuan[2], X. Q. Yuan[37,h], Y. Yuan[1], Z. Y. Yuan[49], C. X. Yue[31], A. A. Zafar[64], X. Zeng Zeng[6], Y. Zeng[19,i], A. Q. Zhang[1], B. X. Zhang[1], Guangyi Zhang[15], H. Zhang[62], H. H. Zhang[26], H. H. Zhang[49], H. Y. Zhang[1,48], J. L. Zhang[68], J. Q. Zhang[33], J. W. Zhang[1,48,53], J. Y. Zhang[1], J. Z. Zhang[1,53], Jianyu Zhang[1,53], Jiawei Zhang[1,53], L. M. Zhang[51], L. Q. Zhang[49], Lei Zhang[34], S. Zhang[49], S. F. Zhang[34], Shulei Zhang[19,i], X. D. Zhang[36], X. Y. Zhang[40], Y. Zhang[60], Y. T. Zhang[70], Y. H. Zhang[1,48], Yan Zhang[62,48], Yao Zhang[1], Z. Y. Zhang[67], G. Zhao[1], J. Zhao[31], J. Y. Zhao[1,53], J. Z. Zhao[1,48], Lei Zhao[62,48], Ling Zhao[1], M. G. Zhao[35], Q. Zhao[1], S. J. Zhao[70], Y. B. Zhao[1,48], Y. X. Zhao[24], Z. G. Zhao[62,48], A. Zhemchugov[28,a], B. Zheng[63], J. P. Zheng[1,48], Y. H. Zheng[53], B. Zhong[33], C. Zhong[63], L. P. Zhou[1,53], Q. Zhou[1,53], X. Zhou[67], X. K. Zhou[53], X. R. Zhou[62,48], X. Y. Zhou[31], A. N. Zhu[1,53], J. Zhu[35], K. Zhu[1], K. J. Zhu[1,48,53], S. H. Zhu[61], T. J. Zhu[68], W. J. Zhu[9,f], W. J. Zhu[35], Y. C. Zhu[62,48], Z. A. Zhu[1,53], B. S. Zou[1], J. H. Zou[1]

(BESIII Collaboration)

[1] Institute of High Energy Physics, Beijing 100049, People's Republic of China

[2] Beihang University, Beijing 100191, People's Republic of China

[3] Beijing Institute of Petrochemical Technology, Beijing 102617, People's Republic of China

[4] Bochum Ruhr-University, D-44780 Bochum, Germany

[5] Carnegie Mellon University, Pittsburgh, Pennsylvania 15213, USA

[6] Central China Normal University, Wuhan 430079, People's Republic of China

[7] China Center of Advanced Science and Technology, Beijing 100190, People's Republic of China

[8] COMSATS University Islamabad, Lahore Campus, Defence Road, Off Raiwind Road, 54000 Lahore, Pakistan

[9] Fudan University, Shanghai 200443, People's Republic of China

[10] G.I. Budker Institute of Nuclear Physics SB RAS (BINP), Novosibirsk 630090, Russia

[11] GSI Helmholtzcentre for Heavy Ion Research GmbH, D-64291 Darmstadt, Germany

[12] Guangxi Normal University, Guilin 541004, People's Republic of China

[13] Hangzhou Normal University, Hangzhou 310036, People's Republic of China

[14] Helmholtz Institute Mainz, Staudinger Weg 18, D-55099 Mainz, Germany

[15] Henan Normal University, Xinxiang 453007, People's Republic of China

[16] Henan University of Science and Technology, Luoyang 471003, People's Republic of China

[17] Huangshan College, Huangshan 245000, People's Republic of China

[18] Hunan Normal University, Changsha 410081, People's Republic of China

[19] Hunan University, Changsha 410082, People's Republic of China

[20] Indian Institute of Technology Madras, Chennai 600036, India

[21] Indiana University, Bloomington, Indiana 47405, USA

[22] INFN Laboratori Nazionali di Frascati , (A)INFN Laboratori Nazionali di Frascati, I-00044, Frascati, Italy; (B)INFN Sezione di Perugia, I-06100, Perugia, Italy; (C)University of Perugia, I-06100, Perugia, Italy

[23] INFN Sezione di Ferrara, (A)INFN Sezione di Ferrara, I-44122, Ferrara, Italy; (B)University of Ferrara, I-44122, Ferrara, Italy

[24] Institute of Modern Physics, Lanzhou 730000, People's Republic of China

[25] Institute of Physics and Technology, Peace Ave. 54B, Ulaanbaatar 13330, Mongolia

[26] Jilin University, Changchun 130012, People's Republic of China

[27] Johannes Gutenberg University of Mainz, Johann-Joachim-Becher-Weg 45, D-55099 Mainz, Germany

[28] Joint Institute for Nuclear Research, 141980 Dubna, Moscow region, Russia

[29] Justus-Liebig-Universitaet Giessen, II. Physikalisches Institut, Heinrich-Buff-Ring 16, D-35392 Giessen, Germany

[30] Lanzhou University, Lanzhou 730000, People's Republic of China

[31] Liaoning Normal University, Dalian 116029, People's Republic of China

[32] Liaoning University, Shenyang 110036, People's Republic of China

[33] Nanjing Normal University, Nanjing 210023, People's Republic of China

[34] Nanjing University, Nanjing 210093, People's Republic of China

[35] Nankai University, Tianjin 300071, People's Republic of China

[36] North China Electric Power University, Beijing 102206, People's Republic of China

[37] Peking University, Beijing 100871, People's Republic of China

[38] Qufu Normal University, Qufu 273165, People's Republic of China

[39] Shandong Normal University, Jinan 250014, People's Republic of China

[40] Shandong University, Jinan 250100, People's Republic of China

[41] Shanghai Jiao Tong University, Shanghai 200240, People's Republic of China

[42] Shanxi Normal University, Linfen 041004, People's Republic of China

[43] Shanxi University, Taiyuan 030006, People's Republic of China

[44] Sichuan University, Chengdu 610064, People's Republic of China

[45] Soochow University, Suzhou 215006, People's Republic of China

[46] South China Normal University, Guangzhou 510006, People's Republic of China

[47] Southeast University, Nanjing 211100, People's Republic of China

[48] State Key Laboratory of Particle Detection and Electronics, Beijing 100049, Hefei 230026, People's Republic of China

[49] Sun Yat-Sen University, Guangzhou 510275, People's Republic of China

[50] Suranaree University of Technology, University Avenue 111, Nakhon Ratchasima 30000, Thailand

[51] Tsinghua University, Beijing 100084, People's Republic of China

[52] Turkish Accelerator Center Particle Factory Group, (A)Istinye University, 34010, Istanbul, Turkey; (B)Near East University, Nicosia, North Cyprus, Mersin 10, Turkey

[53] University of Chinese Academy of Sciences, Beijing 100049, People's Republic of China

[54] University of Groningen, NL-9747 AA Groningen, The Netherlands

[55] University of Hawaii, Honolulu, Hawaii 96822, USA

[56] University of Jinan, Jinan 250022, People's Republic of China

[57] University of Manchester, Oxford Road, Manchester, M13 9PL, United Kingdom

[58] University of Minnesota, Minneapolis, Minnesota 55455, USA

[59] University of Muenster, Wilhelm-Klemm-Str. 9, 48149 Muenster, Germany

[60] *University of Oxford, Keble Rd, Oxford, UK OX13RH*
[61] *University of Science and Technology Liaoning, Anshan 114051, People's Republic of China*
[62] *University of Science and Technology of China, Hefei 230026, People's Republic of China*
[63] *University of South China, Hengyang 421001, People's Republic of China*
[64] *University of the Punjab, Lahore-54590, Pakistan*
[65] *University of Turin and INFN, (A)University of Turin, I-10125, Turin, Italy; (B)University of Eastern Piedmont, I-15121, Alessandria, Italy; (C)INFN, I-10125, Turin, Italy*
[66] *Uppsala University, Box 516, SE-75120 Uppsala, Sweden*
[67] *Wuhan University, Wuhan 430072, People's Republic of China*
[68] *Xinyang Normal University, Xinyang 464000, People's Republic of China*
[69] *Zhejiang University, Hangzhou 310027, People's Republic of China*
[70] *Zhengzhou University, Zhengzhou 450001, People's Republic of China*

[a] *Also at the Moscow Institute of Physics and Technology, Moscow 141700, Russia*
[b] *Also at the Novosibirsk State University, Novosibirsk, 630090, Russia*
[c] *Also at the NRC "Kurchatov Institute", PNPI, 188300, Gatchina, Russia*
[d] *Also at Goethe University Frankfurt, 60323 Frankfurt am Main, Germany*
[e] *Also at Key Laboratory for Particle Physics, Astrophysics and Cosmology, Ministry of Education; Shanghai Key Laboratory for Particle Physics and Cosmology; Institute of Nuclear and Particle Physics, Shanghai 200240, People's Republic of China*
[f] *Also at Key Laboratory of Nuclear Physics and Ion-beam Application (MOE) and Institute of Modern Physics, Fudan University, Shanghai 200443, People's Republic of China*
[g] *Also at Harvard University, Department of Physics, Cambridge, MA, 02138, USA*
[h] *Also at State Key Laboratory of Nuclear Physics and Technology, Peking University, Beijing 100871, People's Republic of China*
[i] *Also at School of Physics and Electronics, Hunan University, Changsha 410082, China*
[j] *Also at Guangdong Provincial Key Laboratory of Nuclear Science, Institute of Quantum Matter, South China Normal University, Guangzhou 510006, China*
[k] *Also at Frontiers Science Center for Rare Isotopes, Lanzhou University, Lanzhou 730000, People's Republic of China*
[l] *Also at Lanzhou Center for Theoretical Physics, Lanzhou University, Lanzhou 730000, People's Republic of China*

Utilizing the data set corresponding to an integrated luminosity of 3.19 fb^{-1} collected by the BESIII detector at a center-of-mass energy of 4.178 GeV, we perform an amplitude analysis of the $D_s^+ \to \pi^+\pi^-\pi^+$ decay. The sample contains 13,797 candidate events with a signal purity of $\sim$80%. We use a quasi-model-independent approach to measure the magnitude and phase of the $D_s^+ \to \pi^+\pi^-\pi^+$ decay, where the $\mathcal{P}$ and $\mathcal{D}$ waves are parameterized by a sum of three Breit-Wigner amplitudes $\rho(770)^0$, $\rho(1450)^0$, and $f_2(1270)$. The fit fractions of different decay channels are also reported.

I. INTRODUCTION

The decay $D_s^+ \to \pi^+\pi^-\pi^+$ is interesting due to its dominant $\mathcal{S}$ wave and relatively large branching fraction [1]. This provides an opportunity to study the structure of the $\pi\pi$ $\mathcal{S}$ wave below 2 GeV and improve our understanding of light scalar mesons such as $f_0(980)$ and $f_0(1370)$, whose exact natures remain a mystery and are open to different interpretations [1]. The $f_0(980)$ is particularly interesting, as it is produced via hadronization of an $s\bar{s}$ quark-antiquark pair close to the $K\bar{K}$ threshold. Its couplings to both $\pi\pi$ and $K\bar{K}$ final states can be studied in decays such as $D_s^+ \to \pi^+\pi^-\pi^+$ and $D_s^+ \to K^+K^-\pi^+$. The study of the $f_0(980)$ line shape can also shed light on its production mechanism [2].

Besides the $\mathcal{S}$ wave component, the amplitude analysis of $D_s^+ \to \pi^+\pi^-\pi^+$ decay can also provide the measurement of the branching fraction of $D_s^+ \to \rho^0\pi^+$, $\mathcal{B}(D_s^+ \to \rho^0\pi^+)$. As pointed out in Ref. [3], the $D_s^+ \to \rho^0\pi^+$ decay is unique because it is the only observed $D \to VP$

mode whose W-annihilation amplitudes for the pseudoscalar meson (P) and vector meson (V) have opposite signs. Both the magnitudes and strong phases of the $A_{P,V}$ amplitudes cannot be determined without the knowledge of the $D_s^+ \to \rho^0\pi^+$ branching fraction. Therefore, $\mathcal{B}(D_s^+ \to \rho^0\pi^+)$ is a crucial experimental input in the global analysis of two-body $D \to VP$ decays in Ref. [3].

Finally, the inclusive decay of D_s^+ into final states including at least three charged pions ($D_s^+ \to \pi^+\pi^-\pi^+X$) is a major background source when measuring $R(D^{*-}) \equiv \mathcal{B}(B^0 \to D^{*-}\tau^+\nu_\tau)/\mathcal{B}(B^0 \to D^{*-}\mu^+\nu_\mu)$, by reconstructing the τ lepton from three charged pions ($\tau^+ \to \pi^+\pi^-\pi^+X$) [4]. Better knowledge on the dynamics of the exclusive $D_s^+ \to \pi^+\pi^-\pi^+$ decay will improve the precision of the $D_s^+ \to \pi^+\pi^-\pi^+X$ decay, and reduce the related systematic uncertainties in the $R(D^{*-})$ measurements.

Amplitude analyses on $D_s^+ \to \pi^+\pi^-\pi^+$ have been performed previously in the E687 [5], E791 [6], FOCUS [7],

and BABAR [8] experiments. BABAR also reported the first model-independent partial wave analysis (MIPWA) on this channel using a large data sample of 13,179 events with a signal purity of 80%. In this paper, based on a 3.19 fb^{-1} data sample collected with the Beijing Spectrometer (BESIII) in 2016 at a center-of-mass energy ($E_{\rm cm}$) of 4.178 GeV, we present an amplitude analysis of $D_s^+ \to \pi^+\pi^-\pi^+$ also based on the MIPWA approach, with a data sample comparable to the one used by BABAR, and a similar purity. At this energy, D_s^+ mesons are produced predominantly through the processes $e^+e^- \to D_s^{*\pm}D_s^{\mp}$. A single D_s^+ (or D_s^-) is reconstructed by its daughter particles. This analysis uses the $D_s^+ \to \pi^+\pi^-\pi^+$ decay and its charge conjugate channel. If one event contains both a D_s^+ and a D_s^- candidate, it will be treated as two events. Charge-conjugate states are implied throughout this paper.

The paper is organized as follows. Section II introduces the BESIII detector and the data and Monte Carlo (MC) simulated samples used in this analysis. Section III gives an overview of the event selection technique and criteria. The details of the $D_s^+ \to \pi^+\pi^-\pi^+$ amplitude analysis are described in Sec. IV, and the fit results are shown in Sec. V. The systematic uncertainties on our measurements are evaluated in Sec. VI, while the final results are summarized in Sec. VII.

II. DETECTION AND DATA SETS

The BESIII detector [9] records symmetric e^+e^- collisions provided by the BEPCII storage ring [10]. BESIII has collected large data samples in this energy region [11]. The cylindrical core of the BESIII detector covers 93% of the full solid angle. Starting from the interaction point (IP), the detector consists of a main drift chamber (MDC), a time-of-flight (TOF) system, a CsI(Tl) electromagnetic calorimeter (EMC) which are all enclosed in a superconducting solenoid magnet providing a 1.0 T magnetic field. The solenoid is supported by an octagonal flux-return yoke with resistive plate counter muon identification modules interleaved with steel. The charged particle momentum resolution at 1 GeV/c is 0.5%, and the dE/dx resolution is 6% for electrons from Bhabha scattering. The EMC measures photon energies with a resolution of 2.5% (5%) at 1 GeV in the barrel (end cap) region. The time resolution in the TOF barrel region is 68 ps, while that in the end cap, that was upgraded in 2015 using multi-gap resistive plate chamber technology, is 60 ps [12].

Simulated data samples are produced with a GEANT4 [13] based MC framework, which includes the geometric description of the BESIII detector and the detector response. The simulation uses the KKMC [14] generator, that takes into account the beam energy spread and the initial-state radiation (ISR) in the e^+e^- annihilations. Used for background study, the inclusive MC sample includes the production of $e^+e^- \to D_s^*D_s$, and other open charm processes, as well as the production of vector charmonium(-like) states, and the continuum processes incorporated in KKMC. The known decay modes are modeled with EVTGEN [15] using branching fractions taken from the Particle Data Group [1], and the remaining unknown decays are modeled with LUNDCHARM [16]. Final state radiation (FSR) from charged final state particles is incorporated using PHOTOS [17].

We also generate a MC sample of $e^+e^- \to D_s^*D_s$ where one D_s decays inclusively, while the other D_s decays into the signal mode according to phase space (PHSP), resulting in a uniformly populated Dalitz plot. This PHSP MC sample is used to evaluate the signal efficiency on the Dalitz plot plane.

III. EVENT SELECTION

To reconstruct the $D_s^+ \to \pi^+\pi^-\pi^+$ decay, we require that three charged track candidates detected in the MDC must be within the polar angle (θ) range of $|\cos\theta| < 0.93$, where θ is defined with respect to the z-axis, which is the symmetry axis of the MDC. The distance of closest approach to the IP is required to be less than 10 cm along the z-axis, $|V_z|$, and less than 1 cm in the transverse plane, $|V_{xy}|$.

Charged tracks are identified as pions or kaons with particle identification (PID), which combines measurements of dE/dx in the MDC and the flight time in the TOF to form likelihoods $\mathcal{L}(h)(h = K, \pi)$ for different hadron h hypotheses. Charged kaons and pions are identified by comparing the likelihoods for the kaon and pion hypotheses, $\mathcal{L}(K) > \mathcal{L}(\pi)$ and $\mathcal{L}(\pi) > \mathcal{L}(K)$, respectively.

Photon candidates are reconstructed using showers in the EMC. The deposited energy of each shower must be more than 25 MeV in the barrel region ($|\cos\theta| < 0.80$) and more than 50 MeV in the end cap region ($0.86 < |\cos\theta| < 0.92$). To exclude showers that originate from charged tracks, the angle between the position of each shower in the EMC and the closest extrapolated charged track must be greater than 10°. Further, the difference between the EMC time and the event start time is required to be within [0,700] ns to suppress electronic noise and showers unrelated to the event.

To identify photons from $D_s^{*+} \to D_s^+\gamma$, we require that the photons are not from any of the reconstructed neutral pions. In the $\pi^0 \to \gamma\gamma$ reconstruction, the photon pair is required to satisfy the above photon selection criteria. The π^0 candidates are selected with the requirement on the invariant mass of the pair of $0.125 < m(\gamma\gamma) < 0.145$ GeV/c^2. This requirement loses $\sim$10% of $D_s^+ \to \pi^+\pi^-\pi^+$ candidates in which $\sim$60% have a photon used in the reconstructed $D_s^{*+} \to D_s^+\gamma$ that is in fact from a π^0.

To suppress pion contributions from $K_S^0 \to \pi^+\pi^-$, we also reconstruct K_S^0 candidates from two oppositely charged tracks satisfying $|V_z| < 20$ cm. The two charged tracks are assigned as $\pi^+\pi^-$ without imposing any PID criteria. They are constrained to originate from a common vertex and required to have an invariant mass within $|m(\pi^+\pi^-) - m_{K_S^0}| < 12$ MeV/c^2, where $m_{K_S^0}$ is the known K_S^0 mass [1]. The decay length of the K_S^0 candidate is required to be greater than twice the vertex resolution away from the IP. Any charged pion candidate that is found to be also part of a reconstructed K_S^0 is rejected. We reduce $D_s^+ \to K_S^0(\to \pi^+\pi^-)\pi^+$ backgrounds to a negligible level ($\sim$0.4%) while retaining 98% of $D_s^+ \to \pi^+\pi^-\pi^+$ signal events.

For each $D_s^+ \to \pi^+\pi^-\pi^+$ candidate, we require the three-pion invariant mass to be between 1.9000 and 2.0535 GeV/c^2. We define the recoil mass of D_s^+ as

$$M_{\mathrm{rec}}c^2 = \sqrt{\left(E_{\mathrm{cm}} - \sqrt{\left|\vec{p}_{D_s^+}c\right|^2 + m_{D_s}^2 c^4}\right)^2 - \left|\vec{p}_{D_s^+}c\right|^2},$$

(1)

where $\vec{p}_{D_s^+}$ is the reconstructed momentum of the D_s^+ candidate (sum of the momenta of three pions) in the e^+e^- center-of-mass frame and m_{D_s} is the known D_s^+ mass [1]. D_s^+ candidates are predominantly from the processes of $e^+e^- \to D_s^\mp D_s^{*\pm}(\to D_s^\pm \gamma)$, which gives D_s^+ that are produced either directly from the e^+e^- collision ("direct D_s^+"), or from D_s^{*+} decay ("indirect D_s^+"). For direct D_s^+ candidates, the M_{rec} distribution will peak around the known D_s^{*+} mass $m_{D_s^*}$, while for indirect D_s^+ candidates, the mass difference $\Delta M \equiv m(D_s^+\gamma) - m(D_s^+)$ will peak around the known mass difference of D_s^{*+} and D_s^+ [1]. We identify the γ from $D_s^{*\pm}$ decay by selecting the one that gives the recoil mass of the $\pi^+\pi^-\pi^+\gamma$ system closest to m_{D_s}.

To suppress background events from mis-combinations of $\pi^+\pi^-\pi^+$ tracks, multivariate classifiers based on artificial neural networks (NNs) [18] are trained separately using different sets of input parameters for the two categories depending on the D_s^+ origin. As in Ref. [19], these two D_s^+ categories are selected on the M_{rec}–ΔM plane. For direct D_s^+ candidates, we require $\left|M_{\mathrm{rec}} - m_{D_s^*}\right| \leq 0.02$ GeV/c^2, and use the following NN input parameters:

- M_{rec};

- P_{rest}, defined as the total momentum of the tracks and neutrals in the rest of event (not part of the $D_s^+ \to \pi^+\pi^-\pi^+$ candidate);

- E_γ, defined as the energy of the photon from a D_s^{*+};

- M'_{rec}, defined as the recoil mass of the $D_s^+\gamma$ combination,

$$M'_{\mathrm{rec}}c^2 = \sqrt{\left(E_{\mathrm{cm}} - \sqrt{\left|\vec{p}_{D_s^+\gamma}c\right|^2 + m_{D_s^*}^2 c^4}\right)^2 - \left|\vec{p}_{D_s^+\gamma}c\right|^2},$$

with $\vec{p}_{D_s^+\gamma}$ as the momentum of $D_s^+\gamma$;

- N_{part}, defined as the total number of charged tracks and photon candidates in an event.

For indirect D_s^+ candidates, we require $\left|M_{\mathrm{rec}} - m_{D_s^*}\right| > 0.02$ GeV/c^2, and $0.135 < \Delta M < 0.15$ GeV/c^2. The following NN input parameters are used in this case:

- ΔM;

- P'_{rest}, defined as the total momentum of the tracks and neutrals in the rest of event (not part of the $D_s^{*+} \to D_s^+\gamma$, $D_s^+ \to \pi^+\pi^-\pi^+$ combination);

- M'_{rec};

- N_{part}.

Our NN response distributions in data and MC samples are compared in Fig. 1 for both D_s^+ categories, where good agreement is observed. The NN response requirements are optimized so that we are able to achieve a signal purity within the signal window (12 MeV, about 2σ, around m_{D_s}) at about the 80% level. With the NN response requirements applied, we perform an unbinned maximum likelihood fit to data, as shown in Fig. 2. The background is modeled by an exponential probability density function (PDF), while the signal is modeled by the sum of a Gaussian PDF and a double-sided Crystal-ball (DSCB) PDF [20] with a common mean value. The DSCB PDF tail parameters, as well as the relative width ratio between the DSCB and Gaussian PDFs, are determined from PHSP MC events and fixed in the fit to data. In total we have 13,797 data events within the signal D_s^+ mass region as shown in Fig. 3, that is slightly more (5%) than BABAR with roughly the same 80% signal purity.

Finally, we perform a kinematc fit to all $D_s^+ \to \pi^+\pi^-\pi^+$ candidates which enforces a D_s^+ mass [1] constraint. The kinematic-fit-corrected 4-momenta of all 3 daughter particles of D_s^+ are used to calculate $\pi\pi$ invariant masses for the following amplitude analysis.

IV. AMPLITUDE ANALYSIS

This analysis will determine the intermediate-state composition of the $D_s^+ \to \pi^+\pi^-\pi^+$ decay by analyzing the Dalitz plot of $D_s^+ \to \pi^+\pi^-\pi^+$ as illustrated in Fig. 3. We take $m^2(\pi^+\pi^-)$ of the two $\pi^+\pi^-$ combinations in $D_s^+ \to \pi^+\pi^-\pi^+$ as x and y axes of the Dalitz plot respectively, while the z ($\equiv m^2(\pi^+\pi^+)$) axis is used later in the efficiency modeling.
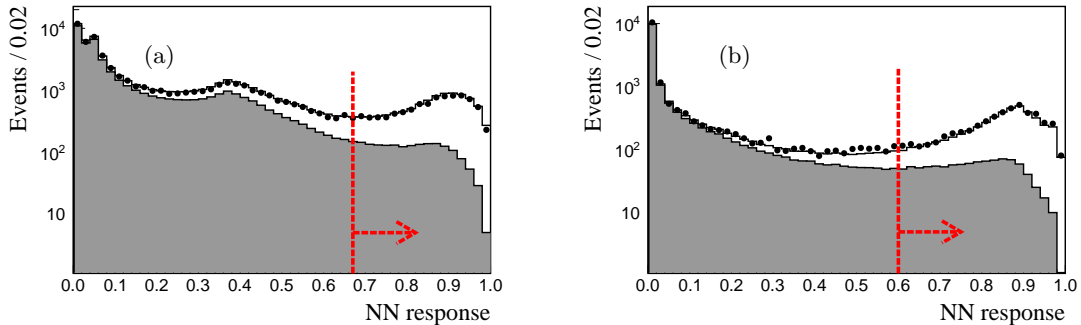
FIG. 1. NN response distributions for (a) direct D_s^+ and (b) indirect D_s^+ categories for data and inclusive MC simulation. The data points are compared to MC simulated histograms including both signal and background (shaded areas) contributions, and are scaled by the integrated luminosity. The requirements on the NN responses are marked by the vertical dashed lines in red.
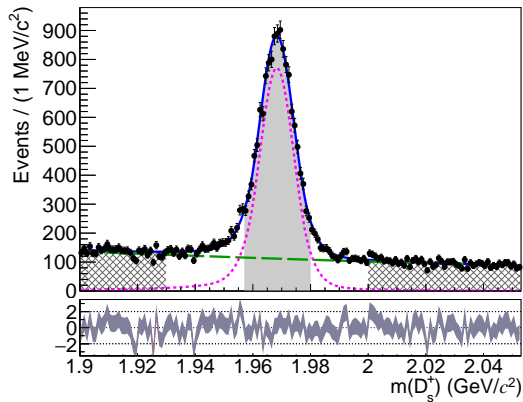
FIG. 2. Fit to the invariant mass distribution of $D_s^+ \to \pi^+\pi^-\pi^+$ candidates $(m(D_s^+))$ of data to determine signal and background yields. Data (points) are shown together with the total fit (blue), signal PDF (magenta dashed), and background PDF (light green long dashed). The $\pm 2\sigma$ signal window corresponds to the shaded region, while the sideband events are taken from the cross-hatched regions.

FIG. 3. Symmetric Dalitz plot of the $D_s^+ \to \pi^+\pi^-\pi^+$ decay from data within the signal region shown in Fig. 2 (with two entries per event).

A. Analysis formalism

The Dalitz plot of $D_s^+ \to \pi^+\pi^-\pi^+$ is described by a coherent sum of three amplitudes corresponding to the $\pi^+\pi^-$ systems with angular momentum quantum numbers $L = 0$, 1, and 2. Each amplitude is symmetrized with respect to the two identical pions in the decay,

$$A^L \left(D_s^+ \to \pi^+\pi^-\pi^+ \right) = A^L(x,y) + A^L(y,x). \quad (2)$$

In our MIPWA formalism, which is similar to that used by the Fermilab E791 Collaboration to model the $K\pi$ $\mathcal{S}$ wave [21], the $\pi^+\pi^-$ $\mathcal{S}$ wave amplitude is a complex function of the $\pi^+\pi^-$ invariant mass $m(\pi^+\pi^-)$. Using the same choice of binning as in Ref. [8], the ampli-

tude $A^0(x,y)$ at 29 control points (k) is described by two real parameters a_k (magnitude) and γ_k (phase). A cubic spline interpolation is used to parametrize $A^0(x,y)$ between the 29 control points,

$$A^0(x,y) = \text{Interp}(a_k \left(m(\pi^+\pi^-) \right) e^{i\gamma_k \left(m(\pi^+\pi^-) \right)})_{k=1,\dots,N}. \quad (3)$$

In total, we have a set of 29 pairs (a_k, γ_k) of fit parameters for the $\mathcal{S}$ wave.

Using the isobar model for $\mathcal{P}$ waves and $\mathcal{D}$ waves, the full amplitude is written as a coherent sum of amplitudes A_i with complex coefficients c_i for the i-th component,

$$\mathcal{A} = c_0 A_0^0 + \sum_i^{L \neq 0} c_i A_i^L , \qquad (4)$$

where $c_0 \equiv 1$, so the free parameters to describe the $\mathcal{S}$ wave component remain unchanged, while the other coefficients c_i ($\equiv |c_i| e^{i\phi_i}$) each has a magnitude $|c_i|$ and a phase ϕ_i for the amplitude A_i^L. Each $\mathcal{P}$ ($\mathcal{D}$) wave amplitude A_i^L is represented by the product of Blatt-Weisskopf barrier factors $F_{D_s,r}^L$ [22], a complex Breit-Wigner function $BW^L (m(\pi^+\pi^-))$ and a real spin-dependent angular term Z^L,

$$A_i^L = F_D^L F_r^L BW^L \left(m(\pi^+\pi^-)\right) Z^L . \qquad (5)$$

The detailed formalism is the same as the one in Ref. [23] and is explicitly written out in Appendix A. For the Blatt-Weisskopf barrier factors, we set the radii of D_s^+ and intermediate resonances to be 5 GeV^{-1} and 1.5 GeV^{-1}, respectively.

B. Efficiency

We model the efficiency across the Dalitz plot for signal events $\eta(x, y) = \mathcal{P}(x, y)\mathcal{T}(x, y)$ as a product of a symmetrical third order two-dimensional polynomial function with respect to the arbitrary point $(x_c, y_c) = (1, 1)$ GeV$^2/c^4$ on the Dalitz plot,

$$\begin{aligned}
\mathcal{P}(x, y) = 1 &+ E_1 \left(\hat{x} + \hat{y}\right) + E_2 \left(\hat{x}^2 + \hat{y}^2\right) + E_{11}\hat{x}\hat{y} \\
&+ E_3 \left(\hat{x}^3 + \hat{y}^3\right) + E_{12} \left(\hat{x}^2\hat{y} + \hat{x}\hat{y}^2\right), \quad (6)
\end{aligned}$$

where $\hat{x} = x - x_c$, $\hat{y} = y - y_c$, and a sine-like threshold factor for each Dalitz plot variable, v ($\equiv x, y$ or z),

$$\mathcal{T}(v) = \begin{cases} \sin(E_{\text{th},v} \cdot |v - v_{\max}|), & E_{\text{th},v} \cdot |v - v_{\max}| < \frac{\pi}{2}, \\ 1, & E_{\text{th},v} \cdot |v - v_{\max}| \geq \frac{\pi}{2}, \end{cases} \qquad (7)$$

where all polynomial coefficients, E_1, E_2, E_{11}, E_3, E_{12}, and $E_{\text{th},v}$ are the fit parameters (requiring $E_{\text{th},y} \equiv E_{\text{th},x}$). Each variable v has one threshold, $v_{\max} \equiv (m_{D_s} - m_\pi)^2$, the kinematic limit of $m^2(\pi\pi)$, where m_π is the known mass of π^+. The fit parameters for the efficiency function $\eta(x, y)$ are determined by fitting to the PHSP MC sample as shown in Fig. 4 and Table I. These fit parameters are fixed in fits to data, while their associated uncertainties are later considered as a source of systematic uncertainties.

TABLE I. Fit results of the efficiency function $\eta(x, y)$ from the PHSP MC sample.

Parameter	Value
E_1	0.064 ± 0.003
E_2	-0.066 ± 0.004
E_3	-0.006 ± 0.002
E_{11}	-0.158 ± 0.006
E_{12}	0.090 ± 0.006
$E_{\text{th},x(y)}$	1.516 ± 0.019
$E_{\text{th},z}$	1.563 ± 0.028

C. Likelihood function construction

We perform an unbinned maximum likelihood fit to the event distribution in the Dalitz plot. This likelihood function is given by

$$\begin{aligned}
\mathcal{L} = \prod_{\text{events}} \Bigg\{ &F \left(m(D_s^+)\right) \eta(x, y) \frac{\sum_{i,j} c_i c_j^* A_i(x, y) A_j^*(x, y)}{\sum_{i,j} c_i c_j^* I_{A_i A_j^*}} \\
&+ \left[1 - F\left(m(D_s^+)\right)\right] \mathcal{B}(x, y) \Bigg\}, \quad (8)
\end{aligned}$$

where

- $F\left(m(D_s^+)\right)$ is the signal fraction, depending on the $\pi^+\pi^-\pi^+$ invariant mass $m(D_s^+)$ before the kinematic fit mentioned in Sec. III. It is defined as

$$F\left(m(D_s^+)\right) = \frac{S\left(m(D_s^+)\right)}{S\left(m(D_s^+)\right) + B\left(m(D_s^+)\right)} ,$$

 where S and B are the signal and background functions used for fitting the data mass distribution as depicted in Fig. 2, respectively;

- $\eta(x, y)$ is the efficiency, parametrized by a third order polynomial function, as defined in Sec. IV B;

- $A_i(x, y)$ describes signal amplitude contribution from the i-th signal component shown in Eq. 4, with the superscript L dropped for simplicity;

- $\mathcal{B}(x, y)$ describes background contribution, which is modeled using data events in the sideband regions ($1.90 < m(D_s^+) < 1.93$ GeV/c^2 and $2.00 < m(D_s^+) < 2.0535$ GeV/c^2). We also have the normalization requirement $\int \mathcal{B}(x, y) dx dy = 1$;

- $I_{A_i A_j^*} = \int A_i(x, y) A_j^*(x, y) \eta(x, y) dx dy$ is the normalization integral for the signal PDF. The integral is calculated numerically based on a large number of PHSP MC events at the generator level.
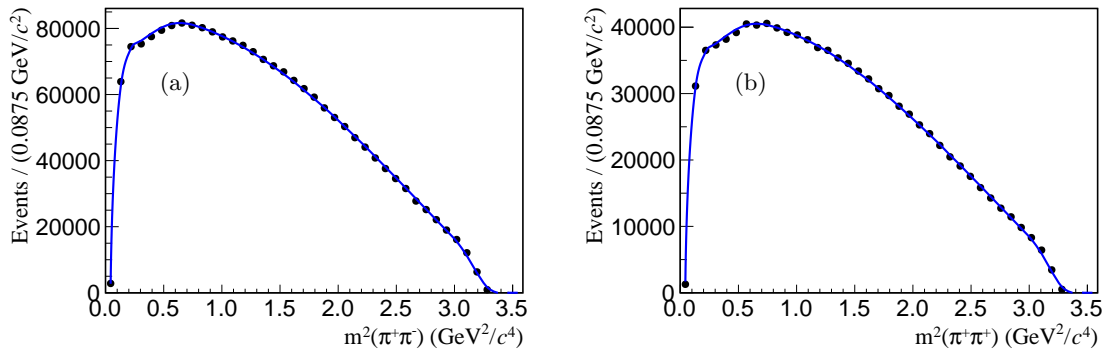
FIG. 4. Dalitz plot projections of PHSP MC events (points) and fit result (blue line) on (a) $m^2(\pi^+\pi^-)$ (two entries per event) and (b) $m^2(\pi^+\pi^+)$ variables.

The fit fraction for the i-th signal component is defined as

$$f_i = \frac{|c_i|^2 \int |A_i|^2 dx dy}{\sum_{j,k} c_j c_k^* \int A_j A_k^* dx dy} \,. \qquad (9)$$

Statistical uncertainties on the fractions include uncertainties on both magnitudes and phases of different signal components, and are computed using the full covariance matrix.

D.   Fitting

Due to the large number of events and many parameters involved for the $\mathcal{S}$ wave parametrization during the Dalitz plot fitting, an open-source framework called `GooFit` [24] has been used to speed up the fitting using the parallel processing power of graphical processing units. The cubic spline interpolation method is implemented based on the `GooFit` framework [25].

V.   RESULTS OF THE MIPWA

As in the previous BABAR analysis with similar data sample size, our baseline signal model includes three intermediate resonances with $L \neq 0$: two $\mathcal{P}$ waves ($\rho(770)$ and $\rho(1450)$) and one $\mathcal{D}$ wave $f_2(1270)$. The partial wave with $f_2(1270)$ is the reference amplitude. With the masses and widths of these three resonances fixed to the world averages, and accounting for the magnitude and phase for each of the 29 $\mathcal{S}$ wave control points, our baseline signal model contains $N_{\mathrm{par}} = 62$ free fit parameters. Tables II and III summarize the results from the amplitude analysis. Our $\mathcal{S}$ wave results are also compared to the BABAR measurements as shown in Fig. 5.

Our fit projections are determined by producing a large number of PHSP MC events at the generator level [15],

which are weighted by the fit likelihood function (Eq. 8), and normalized (with the weighted sum) to the observed number of data events. Good agreement between the data and the fit projections is observed in Fig. 6. As in Ref. [8] for further comparison, we also calculate the unnormalized spherical harmonics moments (Y_l^0), as functions of helicity angle $\theta_{\pi^+\pi^-}$ in the $\pi^+\pi^-$ system, for each $D_s^+ \to \pi^+\pi^-\pi^+$ candidate. The distributions of the $\pi^+\pi^-$ masses (two entries per each candidate) weighted by $Y_l^0(\cos\theta_{\pi^+\pi^-})$ for different l ($l = 1 - 6$) are shown in Fig. 7, where good agreement between the fit and the data is also found.

A.   Goodness-of-Fit

In order to check the goodness-of-fit of our fit results quantitatively, we use a two-dimensional χ^2 test by dividing the Dalitz plot into N_{cells} cells. For the i-th cell, we have $\chi_i = \frac{N_i - N_i^{\mathrm{exp}}}{\sqrt{N_i^{\mathrm{exp}}}}$, where N_i and N_i^{exp} are the observed number of events and expected number of events based on the fit model, respectively. The total χ^2 by summing up χ_i^2 over all cells divided by the number of degrees of freedom (NDF $= N_{\mathrm{cell}} - N_{\mathrm{par}}$, where N_{cell} is the number of cells having entries) is used to quantify the fit quality. In the case of dividing the Dalitz plot equally into 40×40 cells with 768 cells having entries, we have $\chi^2/\mathrm{NDF} = 766.9/(768 - 62)$. We also calculate χ^2 by using an adaptive binning process and requiring the minimal number of entries in each cell is 9, as shown in Fig. 8 which leads to $\chi^2/\mathrm{NDF} = 344.4/(404 - 62)$, with a χ^2 probability of 45%.

VI.   SYSTEMATIC UNCERTAINTIES

We evaluate systematic uncertainties from the following sources:
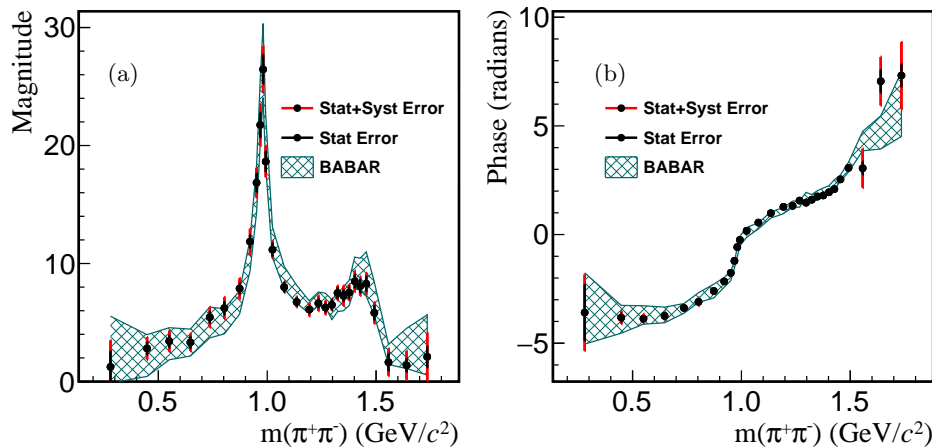
FIG. 5. (a) Magnitudes and (b) phases of the $\mathcal{S}$ wave control points as summarized in Table III. The results are compared to the BABAR results [8] with the same binning scheme and similar data sample size.

TABLE II. Fit fractions, magnitudes and phases from our baseline fit. The uncertainties are statistical and systematic, respectively.

Decay mode	Fit fraction (%)	Magnitude	Phase (radians)
$f_2(1270)\pi^+$	$10.5 \pm 0.8 \pm 1.2$	1. (Fixed)	0. (Fixed)
$\rho(770)\pi^+$	$0.9 \pm 0.4 \pm 0.5$	$0.13 \pm 0.03 \pm 0.04$	$5.44 \pm 0.25 \pm 0.62$
$\rho(1450)\pi^+$	$1.3 \pm 0.4 \pm 0.5$	$0.91 \pm 0.16 \pm 0.22$	$1.03 \pm 0.32 \pm 0.51$
$\mathcal{S}$ wave	$84.2 \pm 0.8 \pm 1.3$	Table III	Table III
Total	$96.8 \pm 2.4 \pm 3.5$		

I The effective barrier radii of mesons R_R and R_D. The related uncertainties are estimated using alternative values of R_R and R_D constants other than the default ones (1.5 GeV^{-1} and $5.0\,\mathrm{GeV}^{-1}$), within the range $[0.0 - 3.0]$ GeV^{-1} and $[3.0 - 7.0]\,\mathrm{GeV}^{-1}$, respectively;

II Amplitude components. We vary resonance masses and widths by $\pm 1\sigma$ from world averages to estimate the related uncertainties;

III Signal efficiency across the Dalitz plot plane. We vary the coefficients used to parametrize Dalitz plot efficiency by $\pm 1\sigma$ (Table I);

IV Background modeling. Instead of the baseline background model with sideband data, similar to that used in Ref. [8], we use a parametrized background PDF by considering contributions from a $\rho(770)^0$ meson, two *ad hoc* scalar resonances with free parameters, and a third order polynomial. The contributions are summed incoherently, and the background PDF parameters are determined by fitting the sideband data and fixed in the amplitude analysis. In addition, we also model the background contribution using events from only the lower or higher sideband regions;

V Method of parameterization of the $\mathcal{S}$ wave. We perform a fit where the $\mathcal{S}$ wave component is parametrized as an interpolation of magnitudes and phases of the 29 control points, instead of their real and imaginary parts. The variations are considered as the related uncertainties;

VI Modeling of ρ resonances. We perform a fit where the ρ mesons are parametrized instead by the Gounaris-Sakurai formalism [26];

VII Alternative signal model. We modify the signal model by adding the $\omega(782)\pi^+$ contribution;

VIII Signal purity. We vary the purity parameter ($F(m(D_s^+))$ in Eq. 8) by $\pm 1\sigma$ (scaling by $\pm 1\%$);

IX Signal window. We fit a different sample of 12,232 data events selected within the 1σ signal window and relaxed requirements on the NN responses. The purity is kept at about the same level as the nominal sample (80%);

X Fit bias. We generate signal MC events using the fitted parameters shown in Tables II and III. The signal MC events are then mixed with signal-removed inclusive MC events to form 35 cocktail MC samples, each with total statistics and signal purity matched to those in data. The parameters of the statistically limited control points that are close to the Dalitz plot kinematic limits have considerable fit biases, which are about the same size

TABLE III. Magnitudes and phases of the $\pi^+\pi^-$ $\mathcal{S}$ wave control points from our baseline fit. The uncertainties are statistical and systematic, respectively.

Point	Mass (GeV/c^2)	Magnitude	Phase (radians)
1	0.280	$1.23 \pm 1.34 \pm 1.79$	$-3.59 \pm 1.29 \pm 1.19$
2	0.448	$2.80 \pm 0.55 \pm 0.76$	$-3.82 \pm 0.20 \pm 0.21$
3	0.550	$3.42 \pm 0.54 \pm 0.70$	$-3.87 \pm 0.15 \pm 0.15$
4	0.647	$3.32 \pm 0.46 \pm 0.56$	$-3.74 \pm 0.15 \pm 0.13$
5	0.736	$5.45 \pm 0.49 \pm 0.70$	$-3.38 \pm 0.12 \pm 0.12$
6	0.803	$6.22 \pm 0.55 \pm 0.73$	$-3.10 \pm 0.13 \pm 0.14$
7	0.873	$7.88 \pm 0.46 \pm 0.73$	$-2.60 \pm 0.12 \pm 0.10$
8	0.921	$11.85 \pm 0.57 \pm 0.94$	$-2.16 \pm 0.12 \pm 0.10$
9	0.951	$16.84 \pm 0.80 \pm 0.98$	$-1.77 \pm 0.11 \pm 0.10$
10	0.968	$21.74 \pm 1.05 \pm 1.41$	$-1.21 \pm 0.11 \pm 0.10$
11	0.981	$26.45 \pm 1.23 \pm 1.55$	$-0.58 \pm 0.11 \pm 0.07$
12	0.993	$18.64 \pm 0.89 \pm 0.98$	$-0.25 \pm 0.10 \pm 0.09$
13	1.024	$11.17 \pm 0.55 \pm 0.47$	$0.17 \pm 0.10 \pm 0.11$
14	1.078	$8.00 \pm 0.42 \pm 0.18$	$0.55 \pm 0.10 \pm 0.07$
15	1.135	$6.74 \pm 0.36 \pm 0.25$	$0.98 \pm 0.09 \pm 0.07$
16	1.193	$6.10 \pm 0.32 \pm 0.46$	$1.28 \pm 0.09 \pm 0.03$
17	1.235	$6.63 \pm 0.38 \pm 0.53$	$1.32 \pm 0.10 \pm 0.03$
18	1.267	$6.27 \pm 0.39 \pm 0.43$	$1.56 \pm 0.11 \pm 0.09$
19	1.297	$6.50 \pm 0.42 \pm 0.25$	$1.47 \pm 0.10 \pm 0.06$
20	1.323	$7.50 \pm 0.47 \pm 0.39$	$1.60 \pm 0.10 \pm 0.07$
21	1.350	$7.27 \pm 0.49 \pm 0.69$	$1.75 \pm 0.10 \pm 0.11$
22	1.376	$7.53 \pm 0.51 \pm 0.45$	$1.80 \pm 0.10 \pm 0.13$
23	1.402	$8.49 \pm 0.56 \pm 0.68$	$1.94 \pm 0.10 \pm 0.07$
24	1.427	$8.08 \pm 0.57 \pm 0.57$	$2.09 \pm 0.11 \pm 0.12$
25	1.455	$8.28 \pm 0.63 \pm 0.64$	$2.54 \pm 0.09 \pm 0.09$
26	1.492	$5.82 \pm 0.60 \pm 0.67$	$3.07 \pm 0.10 \pm 0.12$
27	1.557	$1.64 \pm 0.72 \pm 0.89$	$3.05 \pm 0.30 \pm 0.84$
28	1.640	$1.38 \pm 0.57 \pm 1.07$	$7.06 \pm 0.52 \pm 0.98$
29	1.735	$2.09 \pm 0.89 \pm 1.82$	$7.32 \pm 0.51 \pm 1.44$

as their statistical uncertainties. We take the mean biases observed when fitting to the MC samples as the related uncertainties;

XI Choice of control points. The number of control points used for $\mathcal{S}$ wave modeling has been varied by ± 2 as a consistency check. As no notable variations for the fit parameters are observed, no systematic uncertainty is assigned for this source.

Tables IV and V summarize contributions from the different systematic sources. These contributions are combined in quadrature to determine the total systematic uncertainties.

VII. CONCLUSION

Based on 3.19 fb^{-1} of data taken at $E_{\mathrm{cm}} = 4.178$ GeV with the BESIII detector at the BEPCII collider, we select a sample of 13,797 $D_s^+ \to \pi^+\pi^-\pi^+$ decay events with a signal purity of 80%. The amplitude analysis shows the decay is dominated by the $\pi^+\pi^-$ $\mathcal{S}$ wave. We also observe a significant spin-2 contribution, which is unusual in charm meson decays. Our fit fraction result of $\Gamma(D_s^+ \to$

$\rho^0\pi^+)/\Gamma(D_s^+ \to \pi^+\pi^-\pi^+) = (0.9 \pm 0.4_{\mathrm{stat}} \pm 0.5_{\mathrm{syst}})\%$ shows a central value somewhat lower than that of the BABAR result, however the two results are still compatible within one standard deviation.

Due to the difficulty of using relativistic Breit-Wigner PDFs to model overlapping intermediate scalars such as $f_0(980)$ and $f_0(1370)$, the $\mathcal{S}$ wave content is determined using a quasi-model-independent partial wave analysis method. Our results show good agreement with BABAR with a similar data sample size. The uncertainties of our results are generally better than the BABAR ones. As the same choice of binning on $m(\pi^+\pi^-)$ is used, combining $\mathcal{S}$ wave results from both BESIII and BABAR could offer a very precise description of the $\pi^+\pi^-$ $\mathcal{S}$ wave in the $D_s^+ \to \pi^+\pi^-\pi^+$ decay, which can be later used to test new models for light scalar resonances.
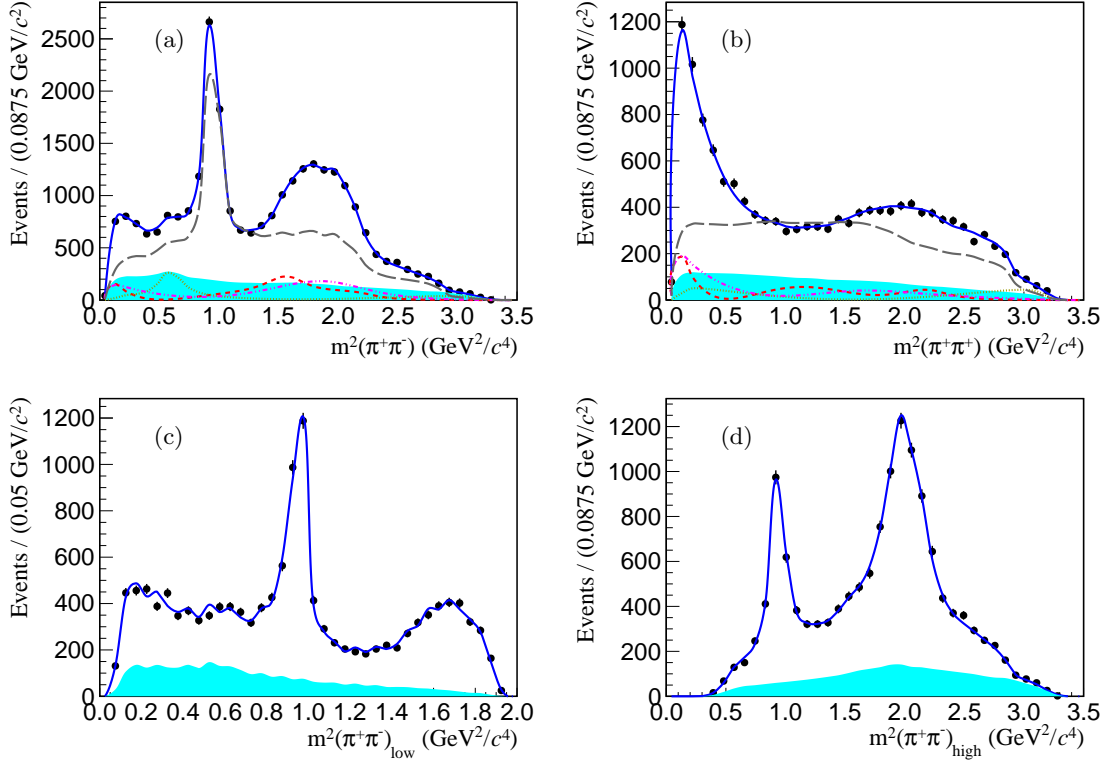
FIG. 6. Dalitz plot projections of data (points with error bars) and total fit results (blue line) on (a) total $m^2(\pi^+\pi^-)$, (b) $m^2(\pi^+\pi^+)$, (c) low mass combination $m^2(\pi^+\pi^-)_{\text{low}}$, and (d) high mass combination $m^2(\pi^+\pi^-)_{\text{high}}$. The shaded areas in cyan represent the background contribution. Also shown in (a) and (b) are contributions from $\mathcal{S}$ wave (gray long-dashed line), $\rho(770)$ (yellow dotted line, scaled by a factor of 10 for better visibility), $\rho(1450)$ (magenta dot-dashed line, scaled by a factor of 10 for better visibility), and $f_2(1270)$ (red short-dashed line).

TABLE IV. Systematic uncertainties for fit fractions and ρ mesons' coefficients. The dominant systematic uncertainties are highlighted in bold.

	I	II	III	IV	V	VI	VII	VIII	IX	X	Total
$f_{f_2(1270)}$ (%)	**0.85**	0.07	0.07	0.35	0.24	0.01	0.02	0.12	0.61	0.00	1.15
$f_{\rho(770)}$ (%)	0.10	0.10	0.06	0.10	0.12	0.05	**0.44**	0.09	0.09	0.11	0.52
$f_{\rho(1450)}$ (%)	**0.42**	0.05	0.05	0.08	0.20	0.04	0.16	0.08	0.05	0.14	0.53
$f_{\mathcal{S}\text{ wave}}$ (%)	**0.67**	0.04	0.10	0.56	0.47	0.06	0.02	0.33	0.64	0.44	1.30
$|c_{\rho(770)}|$	0.01	0.00	0.00	0.00	0.01	0.01	**0.04**	0.01	0.00	0.01	0.04
$\phi_{\rho(770)}$ (rad)	0.09	0.03	0.04	0.26	0.16	0.01	**0.40**	0.04	0.34	0.05	0.62
$|c_{\rho(1450)}|$	0.08	**0.11**	0.02	0.04	0.08	0.10	0.05	0.03	0.05	0.06	0.22
$\phi_{\rho(1450)}$ (rad)	0.09	0.11	0.02	0.05	**0.40**	0.09	0.10	0.10	0.00	0.22	0.51

TABLE V. Systematic uncertainties for the parameters of the $\mathcal{S}$ wave control points. The dominant systematic uncertainties are highlighted in bold.

		I	II	III	IV	V	VI	VII	VIII	IX	X	Total
1	Magnitude	0.96	0.07	0.05	0.48	0.46	0.03	0.08	0.22	0.80	**1.07**	1.79
	Phase (rad)	0.37	0.13	0.02	0.30	0.02	0.10	0.00	0.05	0.42	**0.98**	1.19
2	Magnitude	0.34	0.05	0.05	0.31	**0.44**	0.03	0.05	0.15	0.10	0.35	0.76
	Phase (rad)	**0.17**	0.05	0.01	0.07	0.03	0.02	0.03	0.01	0.04	0.05	0.21
3	Magnitude	0.18	0.05	0.04	0.31	0.33	0.01	0.01	0.16	0.16	**0.45**	0.70
	Phase (rad)	**0.12**	0.03	0.01	0.04	0.03	0.02	0.02	0.00	0.00	0.04	0.15
4	Magnitude	0.11	0.02	0.04	0.30	**0.37**	0.03	0.14	0.15	0.18	0.02	0.56
	Phase (rad)	**0.07**	0.03	0.01	0.05	0.01	0.02	0.06	0.00	0.05	0.04	0.13
5	Magnitude	0.26	0.03	0.05	**0.46**	0.36	0.06	0.02	0.17	0.11	0.19	0.70
	Phase (rad)	0.04	0.01	0.01	0.01	**0.08**	0.02	0.02	0.02	0.01	0.07	0.12
6	Magnitude	**0.43**	0.06	0.06	0.27	0.42	0.02	0.03	0.18	0.02	0.26	0.73
	Phase (rad)	0.03	0.01	0.01	0.03	0.01	0.00	0.04	0.01	0.02	**0.12**	0.14
7	Magnitude	**0.54**	0.07	0.04	0.22	0.31	0.00	0.26	0.13	0.03	0.06	0.73
	Phase (rad)	0.06	0.01	0.01	0.02	0.01	0.01	0.00	0.02	**0.06**	0.03	0.10
8	Magnitude	**0.60**	0.12	0.06	0.25	0.25	0.00	0.01	0.11	0.59	0.09	0.94
	Phase (rad)	0.06	0.02	0.00	0.01	0.02	0.01	0.02	0.01	0.02	**0.07**	0.10
9	Magnitude	**0.65**	0.17	0.08	0.25	0.32	0.01	0.01	0.08	0.56	0.14	0.98
	Phase (rad)	0.05	0.02	0.01	0.01	**0.06**	0.02	0.04	0.01	0.03	0.03	0.10
10	Magnitude	0.69	0.21	0.10	0.27	0.13	0.01	0.06	0.07	**1.15**	0.21	1.41
	Phase (rad)	0.05	0.02	0.01	0.02	0.05	0.02	0.03	0.01	**0.06**	0.01	0.10
11	Magnitude	0.72	0.25	0.11	0.25	0.65	0.00	0.09	0.07	**0.87**	0.74	1.55
	Phase (rad)	**0.05**	0.02	0.01	0.02	0.01	0.02	0.04	0.01	0.01	0.03	0.07
12	Magnitude	0.43	0.18	0.07	0.19	0.03	0.00	0.06	0.06	**0.83**	0.03	0.98
	Phase (rad)	0.05	0.02	0.01	0.02	**0.05**	0.02	0.04	0.01	0.01	0.03	0.09
13	Magnitude	0.15	0.09	0.04	0.19	0.14	0.01	0.04	0.07	**0.35**	0.03	0.47
	Phase (rad)	0.05	0.01	0.00	0.02	**0.08**	0.02	0.03	0.00	0.01	0.04	0.11
14	Magnitude	0.06	0.06	0.02	**0.13**	0.03	0.02	0.03	0.04	0.04	0.03	0.18
	Phase (rad)	0.02	0.01	0.00	0.03	**0.04**	0.01	0.03	0.01	0.02	0.01	0.07
15	Magnitude	0.13	0.05	0.02	0.05	0.11	0.03	0.06	0.02	**0.14**	0.02	0.25
	Phase (rad)	0.01	0.01	0.00	0.04	0.03	0.01	0.02	0.01	**0.05**	0.00	0.07
16	Magnitude	0.12	0.05	0.02	0.07	0.02	0.02	0.04	0.03	**0.42**	0.10	0.46
	Phase (rad)	0.01	0.01	0.00	**0.01**	0.01	0.01	0.01	0.00	0.00	0.01	0.03
17	Magnitude	0.17	0.06	0.02	0.07	0.02	0.01	0.04	0.03	**0.48**	0.08	0.53
	Phase (rad)	**0.02**	0.01	0.00	0.02	0.01	0.01	0.01	0.01	0.00	0.01	0.03
18	Magnitude	0.20	0.05	0.02	0.08	0.07	0.00	0.02	0.03	**0.36**	0.03	0.43
	Phase (rad)	0.02	0.01	0.00	0.01	0.01	0.00	0.01	0.00	**0.08**	0.03	0.09
19	Magnitude	**0.21**	0.05	0.02	0.08	0.05	0.02	0.02	0.04	0.06	0.03	0.25
	Phase (rad)	0.03	0.01	0.00	0.01	0.00	0.00	0.01	0.00	0.01	**0.05**	0.06
20	Magnitude	**0.28**	0.06	0.03	0.08	0.09	0.03	0.00	0.02	0.20	0.10	0.39
	Phase (rad)	**0.04**	0.01	0.00	0.01	0.04	0.00	0.00	0.00	0.03	0.03	0.07
21	Magnitude	0.37	0.06	0.03	0.04	0.03	0.02	0.02	0.01	**0.57**	0.05	0.69
	Phase (rad)	0.05	0.01	0.00	0.02	0.01	0.00	0.01	0.01	**0.07**	0.05	0.11
22	Magnitude	**0.40**	0.07	0.03	0.03	0.01	0.02	0.02	0.00	0.15	0.12	0.45
	Phase (rad)	0.05	0.02	0.00	0.02	0.04	0.00	0.01	0.01	**0.09**	0.06	0.13
23	Magnitude	**0.43**	0.09	0.03	0.06	0.00	0.00	0.03	0.01	0.29	0.43	0.68
	Phase (rad)	**0.06**	0.02	0.00	0.01	0.01	0.00	0.02	0.01	0.02	0.01	0.07
24	Magnitude	**0.44**	0.09	0.03	0.10	0.13	0.01	0.02	0.04	0.28	0.16	0.57
	Phase (rad)	0.07	0.02	0.00	0.01	**0.08**	0.01	0.03	0.02	0.04	0.03	0.12
25	Magnitude	**0.42**	0.10	0.04	0.14	0.11	0.02	0.04	0.04	0.26	0.35	0.64
	Phase (rad)	**0.07**	0.02	0.00	0.01	0.01	0.01	0.03	0.02	0.02	0.02	0.09
26	Magnitude	0.30	0.09	0.04	0.15	0.29	0.00	0.10	0.06	**0.41**	0.27	0.67
	Phase (rad)	**0.07**	0.04	0.00	0.02	0.03	0.02	0.04	0.02	0.07	0.02	0.12
27	Magnitude	0.28	0.19	0.08	0.17	0.42	0.04	0.17	0.05	**0.64**	0.17	0.89
	Phase (rad)	0.32	0.17	0.01	0.23	**0.63**	0.03	0.10	0.23	0.06	0.23	0.84
28	Magnitude	**0.78**	0.19	0.05	0.23	0.17	0.12	0.13	0.14	0.08	0.60	1.07
	Phase (rad)	0.53	0.09	0.06	0.06	**0.60**	0.03	0.07	0.17	0.48	0.21	0.98
29	Magnitude	0.43	0.09	0.05	0.15	0.64	0.05	0.42	0.24	0.34	**1.52**	1.82
	Phase (rad)	0.55	0.03	0.01	0.04	**1.31**	0.05	0.21	0.06	0.09	0.07	1.44
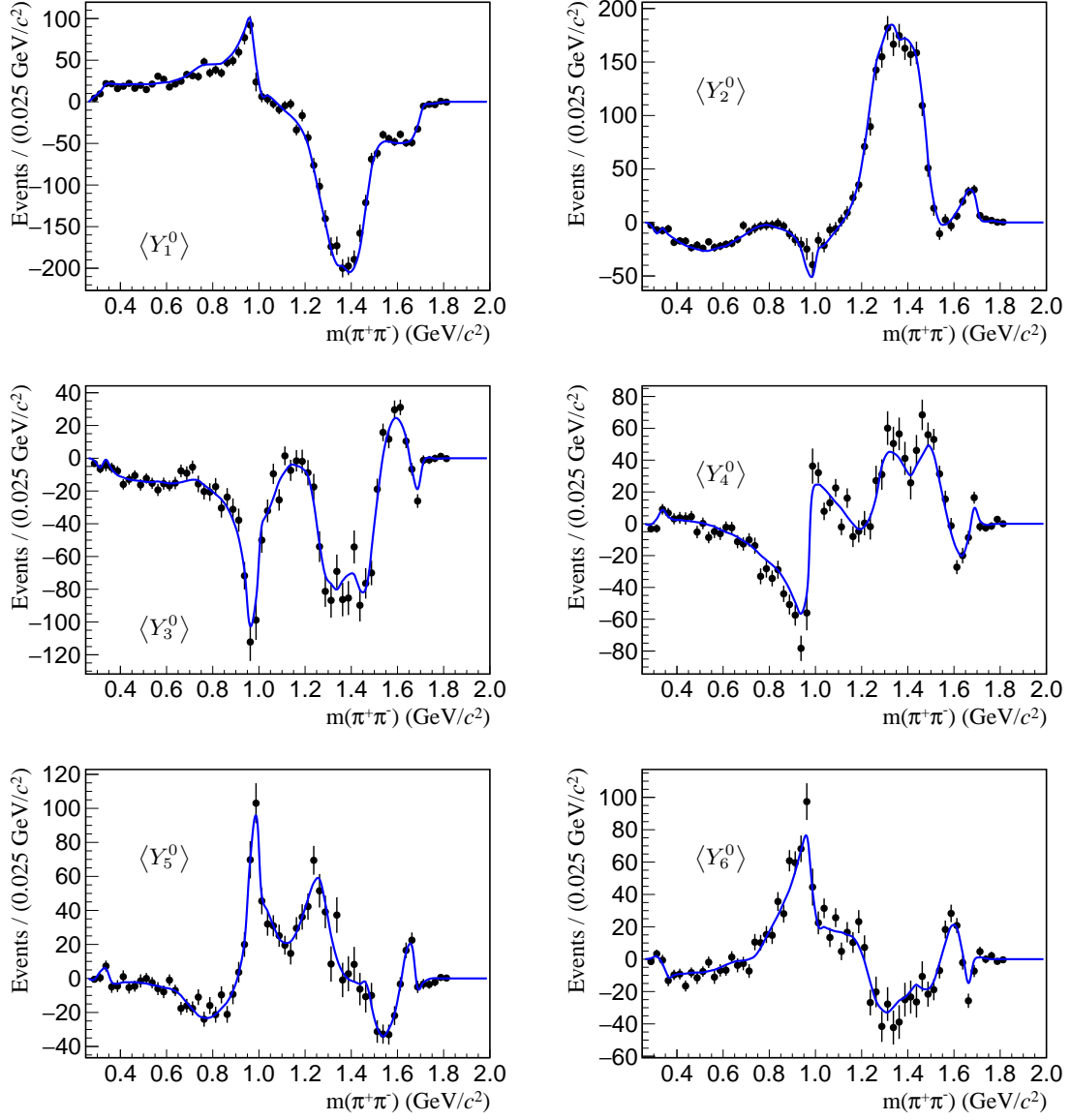
FIG. 7. Unnormalized spherical harmonic moments $\langle Y_l^0 \rangle$ as a function of $\pi^+\pi^-$ invariant mass. Data points are compared to the total fit (blue line). These plots can be compared directly to those in Fig. 4 of Ref. [8].
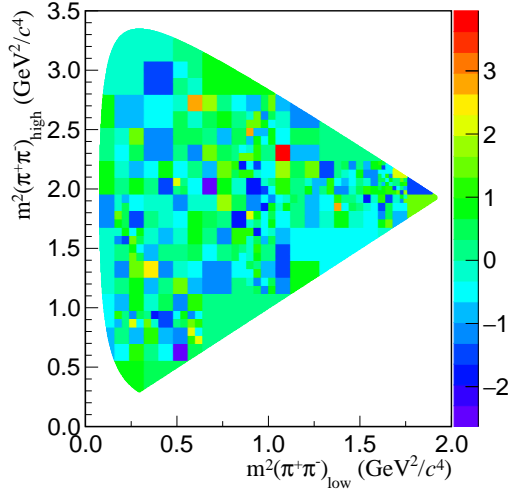
FIG. 8. χ^2 distribution from the fit on the Dalitz plot using the adaptive binning method.

Appendix A: Formalism for amplitudes with $L > 0$

For a D_s^+ meson decaying to three pseudo-scalar mesons via an intermediate resonance r ($D_s^+ \to rC$, $r \to AB$), the amplitude defined in Eq. 5 includes the Blatt-Weisskopf barrier factors F_{D_s} and F_r (Table VI) in an attempt to model the underlying quark structure of the parent particles D_s and r, respectively.

TABLE VI. The Blatt-Weisskopf barrier factors used in this analysis for r in $D_s^+ \to r(\to AB)C$ with different spin L. Here R_{D_s} (R_r) is the effective radius for the D_s^+ (r) decay vertex, q_{AB} (p_{AB}) is the magnitude of the momentum of C (A) in the rest frame of AB, and p_r (q_r) is the value of p_{AB} (q_{AB}) when $m_{AB} = m_r$.

L	F_{D_s}
1	$\sqrt{\dfrac{1+\left(R_{D_s}\cdot q_r\right)^2}{1+\left(R_{D_s}\cdot q_{AB}\right)^2}}$
2	$\sqrt{\dfrac{9+3\left(R_{D_s}\cdot q_r\right)^2+\left(R_{D_s}\cdot q_r\right)^4}{9+3\left(R_{D_s}\cdot q_r\right)^2+\left(R_{D_s}\cdot q_r\right)^4}}$

L	F_r
1	$\sqrt{\dfrac{1+(R_r\cdot p_r)^2}{1+(R_r\cdot p_{AB})^2}}$
2	$\sqrt{\dfrac{9+3(R_r\cdot p_r)^2+(R_r\cdot p_r)^4}{9+3(R_r\cdot p_r)^2+(R_r\cdot p_r)^4}}$

The Breit-Wigner function $BW(m_{AB})$ for the specific process $r \to AB$ has the form:

$$BW^L(m_{AB}) = \frac{1}{m_r^2 - m_{AB}^2 - im_r\Gamma^L(m_{AB})}, \quad \text{(A1)}$$

where $\Gamma^L(m_{AB})$ is a function of the invariant mass of AB system m_{AB}, p_{AB}, the spin L, the mass m_r and the width Γ_r of the resonance r. The explicit form is

$$\Gamma_{AB}(m_{AB}) = \Gamma_r \left(\frac{p_{AB}}{p_r}\right)^{2L+1} \left(\frac{m_r}{m_{AB}}\right) F_r^2, \quad \text{(A2)}$$

The angular terms Z^L for $\mathcal{P}$ and $\mathcal{D}$ waves are described by the following expressions,

$$L = 1 : Z = m_{BC}^2 - m_{AC}^2$$
$$- \frac{(m_{D_s}^2 - m_C^2)(m_B^2 - m_A^2)}{m_{AB}^2}, \quad \text{(A3)}$$
$$L = 2 : Z = a_1^2 - \frac{1}{3}a_2 a_3,$$

where a_1, a_2, and a_3 are defined as

$$a_1 = m_{BC}^2 - m_{AC}^2 + \frac{(m_{D_s}^2 - m_C^2)(m_A^2 - m_B^2)}{m_{AB}^2},$$
$$a_2 = m_{AB}^2 - 2m_{D_s}^2 - 2m_C^2 + \frac{(m_{D_s}^2 - m_C^2)^2}{m_{AB}^2}, \quad \text{(A4)}$$
$$a_3 = m_{AB}^2 - 2m_A^2 - 2m_B^2 + \frac{(m_A^2 - m_B^2)^2}{m_{AB}^2}.$$

Here, m_{BC} and m_{AC} are the invariant mass of the BC and AC systems, respectively, and m_A, m_B, and m_C denote the masses of A, B, and C (all equal to m_π in our case).

[1] P. A. Zyla *et al.* (Particle Data Group), Prog. Theor. Exp. Phys. **2020**, 083C01 (2020).
[2] J. M. Dias, F. S. Navarra, M. Nielsen and E. Oset, Phys. Rev. D **94**, 9, 096002 (2016).
[3] H. Y. Cheng, C. W. Chiang and A. L. Kuo, Phys. Rev. D **93**, 114010 (2016); H. Y. Cheng and C. W. Chiang, Phys. Rev. D **100**, 093002 (2019); H. Y. Cheng and C. W. Chiang, arXiv:2104.13548.
[4] R. Aaij *et al.* (LHCb Collaboration), Phys. Rev. Lett. **120**, 171802 (2018); R. Aaij *et al.* [LHCb Collaboration], Phys. Rev. D **97**, 072013 (2018).
[5] P. L. Frabetti *et al.* (E687 Collaboration), Phys. Lett. B **407**, 79 (1997).
[6] E. M. Aitala *et al.* (E791 Collaboration), Phys. Rev. Lett. **86**, 765 (2001).
[7] J. M. Link *et al.* (FOCUS Collaboration), Phys. Lett. B **585**, 200 (2004).
[8] B. Aubert *et al.* (BABAR Collaboration), Phys. Rev. D **79**, 032003 (2009).
[9] M. Ablikim *et al.* (BESIII Collaboration), Nucl. Instrum. Methods Phys. Res., Sect. A **614**, 345 (2010).
[10] C. H. Yu *et al.*, Proceedings of IPAC2016, Busan, Korea, 2016, doi:10.18429/JACoW-IPAC2016-TUYA01.
[11] M. Ablikim *et al.* (BESIII Collaboration), Chin. Phys. C **44**, 040001 (2020).
[12] X. Li *et al.*, Radiat. Detect. Technol. Methods **1**, 13 (2017); Y. X. Guo *et al.*, Radiat. Detect.Technol. Methods **1**, 15 (2017); P. Cao *et al.*, Nucl. Instrum. Meth. A **953**, 163053 (2020).
[13] S. Agostinelli *et al.* (GEANT4 Collaboration), Nucl. Instrum. Methods Phys. Res., Sect. A **506**, 250 (2003).
[14] S. Jadach, B. F. L. Ward and Z. Was, Phys. Rev. D **63**, 113009 (2001).
[15] D. J. Lange, Nucl. Instrum. Methods Phys. Res., Sect. A **462**, 152 (2001); R. G. Ping, Chin. Phys. C **32**, 599 (2008).
[16] J. C. Chen *et al.*, Phys. Rev. D **62**, 034003 (2000); R. L. Yang *et al.* Phys. Lett. **31**, 061301 (2014).
[17] E. Richter-Was, Phys. Lett. B **303**, 163 (1993).
[18] H. Voss, A. Hoecker, J. Stelzer, and F. Tegenfeldt,

Proc. Sci., ACAT 040 (**2007**); A. Hoecker *et al.*, arXiv:physics/0703039.

[19] M. Ablikim *et al.* (BESIII Collaboration), Phys. Rev. D **104**, 012006 (2006).

[20] T. Skwarnicki, Ph.D. thesis, Institute of Nuclear Physics, Krakow Poland, 1986 [DESY Report No. DESY-F31-86-02, 1986 (unpublished)].

[21] E. M. Aitala *et al.* (E791 Collaboration), Phys. Rev. D **73**, 032004 (2006).

[22] J. M. Blatt and V. F. Weisskopf, *Theoretical Nuclear Physics* (Wiley, New York, 1951), p. 361.

[23] P. del Amo Sanchez *et al.* (BABAR Collaboration), Phys. Rev. D **83**, 052001 (2011).

[24] R. Andreassen *et al.*, IEEE Access **2**, 160 (2014).

[25] L. Sun *et al.*, J. Phys. Conf. Ser. **898**, 072025 (2017).

[26] G. J. Gounaris and J. J. Sakurai, Phys. Rev. Lett. **21**, 244 (1968).